Superlattices in van der Waals materials: a low-energy electron microscopy study

Jong, T.A. de

5

ON STACKING CONTRAST OF LOW ENERGY ELECTRONS IN MULTILAYER GRAPHENE

Parts of this chapter are under review as T. A. de Jong, X. Chen, E. E. Krasovskii, R. M. Tromp, J. Jobst & S. J. van der Molen, Low-Energy Electron Microscopy contrast of stacking boundaries: comparing twisted few-layer graphene and strained epitaxial graphene on silicon carbide [124]

5.1 INTRODUCTION

In the previous chapter we have shown that Dark Field LEEM can be used to image stacking domains in bilayer and trilayer graphene on SiC. Tilted DF-LEEM was used, as the rotational equivalency between AB and AC stacking means no contrast can be expected in Bright Field LEEM. However, the domain boundaries themselves can be imaged in BF-LEEM, as is already visible in for example Figure 4.6**c,d** and Figure 3.11**b**. In this chapter, we will explore the contrast mechanisms enabling this. To do so, the intensity of the domain boundaries needs to be separated from the domains themselves, which is non-trivial because the domain boundaries are a few pixels wide at most. Improving on the PCA-based method used in Section 3.5.2, we will here average over multiple unit cells to increase the resolution and signal-to-noise ratio and extract the contrast information as a function of E_0 we need. We will use this information to compare domain boundaries in graphene on SiC with the similar domain boundaries occurring in twisted bilayer graphene. First the material systems and precise type of domain boundaries occurring in them are discussed, before the averaging method and the results.

5.1.1 GRAPHENE ON SILICON CARBIDE

Graphene on silicon carbide (SiC(0001)) is grown by thermal decomposition. As silicon has a lower sublimation point than carbon, heating an atomically flat surface of SiC to 1200°C or higher, the silicon evaporates, while the carbon stays behind [12, 125]. Every three layers of carbon of the original SiC crystal form a single layer of hexagonal carbon [126]. Growing the graphene at higher temperatures or keeping it hot for longer causes more silicon to evaporate and extra layers to form between the buffer layer and the lowest graphene layer [127]. This growth is faster and less regular on the carbon face of the SiC than on the Si face, and here we will focus on growth on the Si face. To create more regular layers, a gas backpressure of silane [114] or, more commonly, argon of up to one bar can be supplied. This achieves more uniform growth at lower speeds and higher temperatures [95]. Additionally, extra carbon can be provided by depositing carbon in advance [10, 128].

There are several benefits in this growth method compared to the alternative, graphene growth on metals. The main advantage is that the growth is epitaxial, and therefore results in a single orientation of graphene, while for all metal growth procedures step edges, metal grains and multiple possible growth orientations will cause domains of varying orientation. Furthermore, SiC wafers integrate well in the semiconductor industry, making wafer-scale applications easier to implement.

However, the lattice constant of hexagonal carbon does not match the lattice constant of SiC. Thus a higher-order commensurate reconstruction, i.e. a moiré pattern is formed, denoted by $\left(6\sqrt{3}\times 6\sqrt{3}\right)R30°$ [12, 13].

The first layer of hexagonal carbon is covalently bonded to the SiC surface. This means this so-called buffer layer is insulating due to the lack of pure sp^2 hybridization and that it adheres perfectly to the higher-order commensurate reconstruction. All subsequent carbon layers are true graphene layers and thus only bonded to the lower layers by Van der Waals forces. Aside from the implications for the conduction, this also implies that the graphene layer on top of the buffer layer has much lower interlayer interaction energies than the buffer layer with respect to the SiC substrate. Therefore, any residual

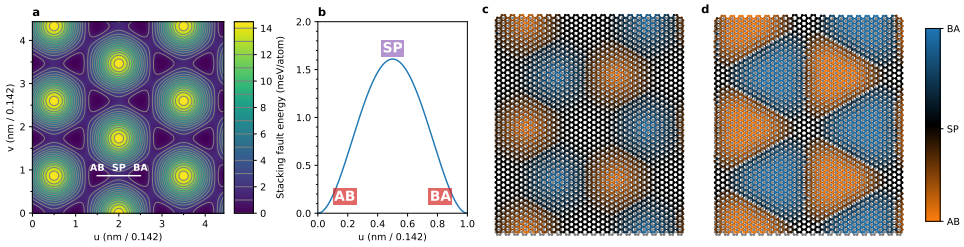

Figure 5.1: ***a,*** *Approximate interlayer stacking energy (in meV/atom) for bilayer graphene as a function of relative displacement in units of the graphene bond length $l_0 = 0.142\,nm$, as given in Ref. [19]. (cf. calculated energy in Ref. [11]). Note that the stacking energy for AA stacking relative to Bernal stacking (AB/BA) is around 9 times higher than the maximum occurring in a domain wall, which is labeled SP (for saddle point).* ***b,*** *Least energy cut through the energy landscape as indicated in* ***a****, from AB to BA stacking across the saddle point.* ***c,*** *Schematic of two unrelaxed hexagonal lattices with slightly different lattice constant.* ***d,*** *As Bernal stacking (AB/BA) is energetically favorable compared to other stackings, the bilayer will relax to form triangular Bernal stacked domains with all strain concentrated in the boundaries.*

lattice constant mismatch between graphene and the $\left(6\sqrt{3}\times 6\sqrt{3}\right)R30°$ reconstruction of the buffer layer can be resolved, especially at the high growth temperatures.

As the buffer layer is similar to a graphene layer, the interlayer stacking energy landscape should be similar to that of bilayer graphene, which is shown in Figure 5.1**a**. Here, the Bernal stackings (AB/BA)[1] are the energy minima. When one of the layers is shifted to form AA stacking, this corresponds to a maximum. For a small residual lattice mismatch, schematically shown in Figure 5.1**c**, the relative stacking and therefore the local interlayer stacking energy varies continuously as a function of position. When relaxing this structure, the interlayer stacking energy will be minimized at the cost of some stretching of the layer. Now, triangular domains form, where in each boundary the strain is concentrated (Figure 5.1**d**), and the stacking varies smoothly, going from one Bernal minimum to the other via the saddle point (SP) in the energy landscape (Figure 5.1**b**).

Indeed, in Chapter 4, we have shown that the residual lattice mismatch at the growth temperature causes such stacking domains between the (intercalated) buffer layer and the subsequent graphene layer [129, 130], with an influence on the (de-)intercalation process. The morphology and variety of the domains and the connection to strain and defects is explored in more depth in Chapter 7.

5.1.2 TWISTED FEW-LAYER GRAPHENE

In twisted few-layer graphene made by mechanical exfoliation, the lattice mismatch is not due to an intrinsic mismatch of the lattice constant of the graphene with respect to that of the substrate, but by artificially rotating the top layers by a twist angle θ with respect to the bottom layers.

[1] As stacking labels correspond to the sublattice labels, which can be freely permuted when labeling bilayers, AB, BC and CA are equivalent, as are AC, BA and CB. While technically one can argue that in the case of graphene on SiC the buffer layer is commensurate to the substrate and should therefore maintain the same label, for simplicity we will use AB and BA for the two different Bernal stackings in this chapter.

Here, a continuous transition from the commensurate case at $\theta = 0$ to the incommensurate case for twist angles larger than a critical angle occurs. This critical angle depends on the precise number of layers. Here, precise estimates of the critical angle vary, with estimates for the 1-on-1 layer case between about 1 and 2 degree [120, 129].[2] Below the critical angle, locally commensurate stacking domains form, with all strain concentrated in domain boundaries [129, 130]. However, these domain boundaries are qualitatively different for the twisted case compared to the biaxially strained case: while in the strained case the lattice mismatch or displacement compensated by the domain boundary is perpendicular to the so-called **tensile** domain boundary, in the twisted case this is parallel to the so-called **shear** domain boundary.

In the more general case of mixed twist and (uniaxial) strain, mixes between these two types also occur. Applying the two chain Frenkel-Kontorova model to bilayer graphene, Lebedeva and Popov found that the shear domain boundary has a slightly lower total energy cost per unit length than the tensile boundary [19]. They also calculated a width of 13.4 nm for the tensile domain wall and 8.6 nm for the shear domain wall. These values match experimental values of 11 nm and 6–7 nm measured using TEM [106, 131] to within the expected accuracy of their model.

Both in the twisted case and in the biaxially strained case, domain boundaries that occur at different azimuthal angles have to cross. In bilayer graphene, such a domain boundary crossing corresponds to AA-stacking, and is therefore called an AA-node.

Notably, in the twisted case, such domain boundary stackings are in some sense topologically protected: short of destroying the lattice by adding or removing atoms, they can only be destroyed by moving them all the way to the edge of the system. As they therefore exhibit particle-like properties, they are sometimes called **twistons** [132]. Similar properties hold in the strained case, and therefore we mint the term **strainons** for AA-nodes in graphene on SiC.

As AA stacking corresponds to a maximum in the stacking energy, domain boundary crossings have an extra energy cost. When that energy cost is higher than the cost of absorbing the strain to a commensurate stacking in one direction, a stripe phase occurs where the strain is concentrated in domain boundaries in only one direction [19].

5.1.3 IMAGING DOMAIN BOUNDARIES

There are several reasons to study domain boundaries in twisted and strained systems. A first reason is to accurately measure the atomic lattice mismatch of the constituting systems. A second reason is that the domain boundaries may have effects on physical properties of the system, as is the case for hydrogen (de-)intercalation of graphene on SiC (Chapter 4) and the existence of edge states along the domain boundary [108, 122, 133, 134]. A final reason, employed in Ref. [17] as well as in Chapters 6 and 7, is that the domain boundary patterns magnify the local relative differences of the lattices, enabling imaging of local strain and deformations. This includes local topological atomic defects, which are magnified in the domain boundary pattern, in particular edge dislocations. Thus, such defects can be made visible without imaging the atomic lattice directly.

[2] Notably, this critical angle and the first magic angle for bilayer graphene are very close. What is more, for additional layers, both angles increase.

In this chapter, we use Bright Field Low Energy Electron Microscopy (BF-LEEM) to characterize the contrast of domain boundaries in both twisted graphene systems and in the strained graphene on (buffer layer on) SiC and subsequently compare them [25, 27, 37, 135]. In Chapter 7, the domain boundaries are used to extract information about the influences that different growth procedures may have on the interlayer interaction and the local disorder this produces.

5.2 STACKING CONTRAST OF BILAYERS IN LEEM

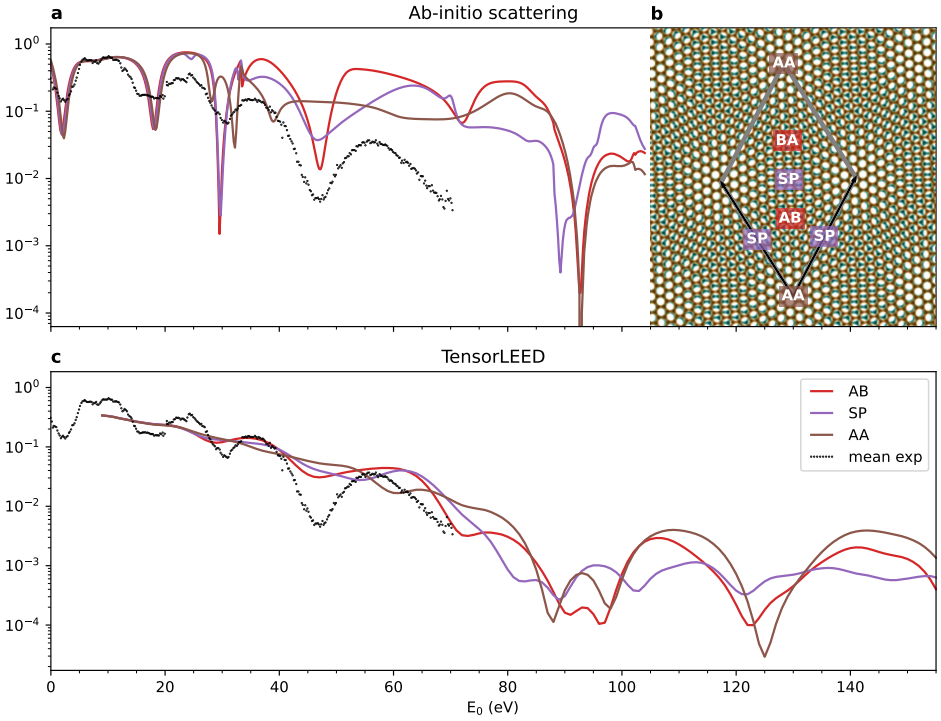

Figure 5.2: ***a,*** *Calculated electron reflectivity with the ab-initio Bloch-wave-based scattering method described in Ref. [136] for different bilayer graphene stackings as calculated by E.E. Krasovskii. The different relative shifts of the two graphene layers correspond to different positions within the unit cell. In black dots, the mean reflectivity of* $\theta \approx 0.18^\circ$ *TBG on hBN is overlayed for comparison.* ***b,*** *TBG unit cell schematic with positions where the different stackings occur labeled.* ***c,*** *Similar as a, but calculated using tensorLEED, from ref. [137].*

In Dark Field LEEM (DF-LEEM), the rotational equivalence between the two possible Bernal stackings, AB and BA, is broken, causing contrast between the domains themselves [37, 138]. In BF-LEEM, both Bernal stackings are fully equivalent by rotation and no contrast between them can be expected, but the domain boundaries themselves do cause contrast. To understand the domain boundary contrast observed with LEEM we

would like to compare measurements to theoretical calculations. Unfortunately, the super cells, both of twisted bilayer graphene at angles near the magic angle and of any reasonable lattice mismatch caused by strain, contain too many atoms to be amenable to reflectivity calculations using conventional methods. A simplifying assumption to tackle the problem would be that for large enough unit cells, the main contrast mechanism is due to stacking contrast, e.g. the different local stackings in the super cell having slightly different electron reflectivities as a function of landing energy, causing visible contrast to image the super cells. Here any lateral interaction between the different areas in the unit cell is ignored, which is equivalent to assuming pure amplitude contrast and no phase contrast [139].

To test this assumption, we compare experimentally observed contrast to ab-initio calculations from different sources: an ab-initio Bloch-wave-based scattering method computed by E.E. Krasovskii [135, 140] and traditional tensorLEED calculations as reported in Ref. [137]. Computed reflectivity curves from both methods are shown in Figure 5.2, together with an indication of where the different stackings occur in the unit cell of TBG.

Both calculations predict very little contrast between different stackings at landing energies lower than the appearance of the first order diffraction spots, i.e. $E_0 \lesssim 30\,\text{eV}$. The contrast increases for higher E_0. However, two things should be noted here. First, the so-called muffin tin approximation used in tensorLEED severely limits its accuracy at low energies. The ab-initio scattering method is much more accurate in this energy regime. Remarkably, the difference between the different stackings in the ab-initio scattering calculations seems to be limited to a small shift along energy, i.e. a slight work function difference. The second thing to note is that although high contrast is predicted for higher energies, in experimental practice, the measured contrast for higher energies is decreased by both inelastic losses, causing broadening of the measured spectra, and decreasing intensity, causing decreased signal-to-noise ratios. This means that a priori, it is not clear from these calculations what would be the optimal energy to measure such stacking contrast.

5.2.1 UNIT CELL AVERAGING

To further complicate comparison to experiment, the width of a single domain boundary is too small to accurately sample at a single position, making comparison to the calculated reflectivity of different stackings for different regions of interest impractical.[3]

Therefore, to optimally compare experiment and theory, we will try to average data over multiple unit cells of the moiré lattice. However, in general, strain and twist angle variation will cause deformation of the unit cell, which means we can not just project back into the unit cell by shifting pixels over integer multiples of the unit vectors. Instead, as illustrated in Figure 5.3, we should first correct the deformation due to strain and twist angle, which we can do by calculating the displacement field $\mathbf{u}(\mathbf{r})$ (green arrows in Figure 5.3**a**) using geometric phase analysis (See Appendix A), such that $\mathbf{r}' = \mathbf{r} + \mathbf{u}(\mathbf{r})$ with $\mathbf{r}'$ the corresponding position in the *undistorted* lattice. This can then be used to perform a Lawler-Fujita type distortion correction [135, 141–143], where an undistorted image is

[3] In fact, the domain boundaries might be too thin to observe at all in non-aberration corrected LEEM, as attempts using microscopes without aberration correction have so far been unsuccessful.

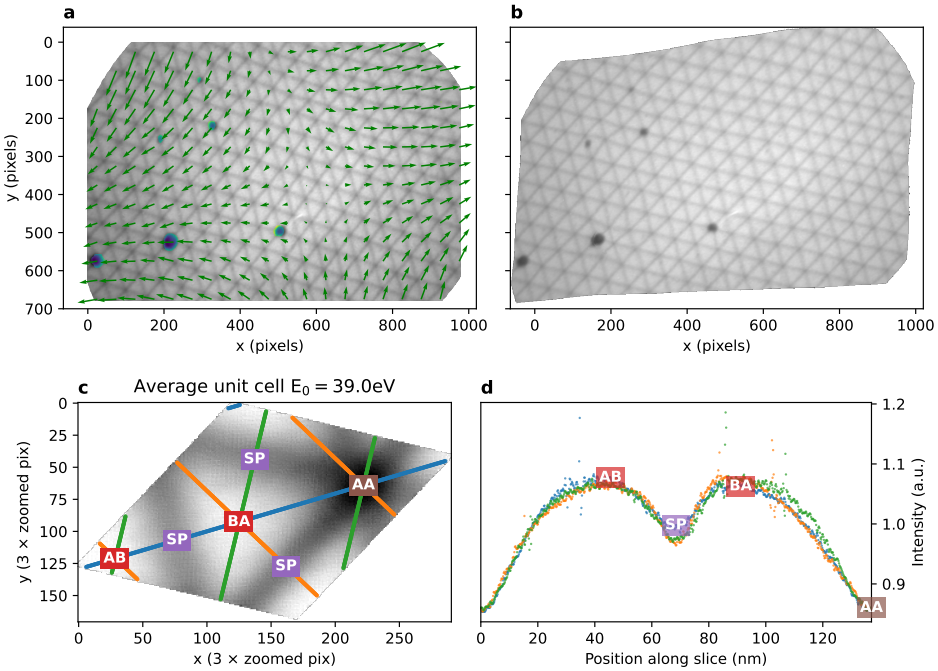

Figure 5.3: Unit cell averaging. ***a,*** *From a displacement field* $\mathbf{u}(\mathbf{r})$ *calculated using GPA (green arrows), we can compute a corrected regular lattice as shown in* ***b****. This regular lattice can be averaged by projecting into a single unit cell* ***c*** *by subtracting integer multiples of the lattice vectors.* ***d,*** *To visualize the unit cell as a function of energy, equivalent cuts in different directions along the unit cell can be made. Colors match the indicated slices in* ***c*** *and Figure 5.4. Spikes in the intensity are due to incorrect handling of the edges of the unit cell (See Section 5.6) and are filtered out in the results. The image used for illustration here is the* $\theta \approx 0.18°$ *TBG sample also used in Figure 5.4.*

sampled from positions $\mathbf{r}' + \mathbf{u}^{-1}(\mathbf{r}')$ by interpolation, where $\mathbf{u}^{-1}$ is determined by approximation or by numerical inversion. Of the resulting image, shown in Figure 5.3**b**, it is now possible to project all cells into a single unit cell (Figure 5.3**c**) by integer multiples of the unit vectors:

$$\mathbf{r}_p = \left(A^{-1}\mathbf{r}\right) \mod 1$$

Here, A is the matrix with the lattice vectors as columns, such that A^{-1} converts to coordinates in terms of the lattice vectors.

However, this two-step process would cause interpolation errors twice and is unsuited for upscaling of the unit cell to recover more detail. Fortunately, once $\mathbf{u}(\mathbf{r})$ is known, we can directly compute the precise (i.e. sub-pixel coordinates) position inside the unit cell for each pixel in the original image:

$$\mathbf{r}_p = \left(A^{-1}(\mathbf{r} + \mathbf{u}(\mathbf{r}))\right) \mod 1$$

Therefore we can directly combine all pixels of the original image (Figure 5.3**a**) into an average unit cell (**c**), scaling up and using a 'drizzle' like [144, 145] approach to minimize the smoothing caused by the recombination and we may even hope to recover some additional detail not apparent from the original images.[4]

The process described above allows us to compute a single average unit cell from an image with distortion, provided that the moiré contrast and signal-to-noise ratio are high enough. By doing this for all images in a spectroscopic LEEM dataset, we can obtain the average unit cell reflectivity as a function of E_0. However, the contrast of the moiré will be essentially zero for some energies, causing the extraction of the distortion field to fail. We also need to exclude areas with significant (dirt) artefacts. Furthermore, the area used for averaging should be limited to an area with approximately constant distortion, as the contrast may depend on the distortion. For example, domain boundaries have an approximately constant width, independent of unit cell size and distortion, which is thus distorted when projecting back different size unit cells to a single unit cell. Accommodating these complications, the unit cell averaging process we use is as follows:

0. Properly correct the dataset for detector artefacts and drift.
1. Compute $\mathbf{u}(\mathbf{r})$ with respect to an isotropic lattice for a value of E_0 where the contrast of the moiré is high enough. Preferably use an image consisting of the average over a few images around that energy to minimize noise.
2. Determine the high symmetry point (in practice the AA site) from the same image. This is used to take one-dimensional slices of the data later on.
3. Mask out any adsorbates and otherwise unwanted areas. In implementation, this is done by converting any such areas to NaNs and explicitly ignoring NaNs in the actual unit cell averaging.[5]
4. Use the same distortion field $\mathbf{u}(\mathbf{r})$ to compute an average unit cell for all landing energies.
5. Take appropriate slices through the unit cells that enumerate the theoretically computed stackings.
6. To cancel out disagreements between models and experimental data in the global intensity, divide these cuts by some reference stacking, in this case Bernal stacking. In the following, if this is not feasible due to remaining detector drift, we divide by the average spectrum instead. Finally, for comparison, we take the natural logarithm of the result.

The core unit cell averaging algorithm is written in Python and made available as part of `pyGPA` [88], and the Python code used to generate the figures in this Chapter is available at Ref. [146].

[4] The amount of detail within the unit cell that can be recovered in this way depends on the ratio between the pixel pitch and the width of the contrast transfer function (CTF) of the instrument. Therefore this technique might be applied with much more result to experiments where this ratio is large, such as large field-of-view STM, STEM, or AFM measurements.

[5] For simplicity, any area where data is missing for any value of E_0 due to detector drift is ignored, although this could in theory be used for the energies where data exists.

5.2.2 TWISTED BILAYER GRAPHENE RESULTS

The unit cell averaging procedure introduced in the previous section is applied to a dataset of twisted bilayer graphene (TBG), with a twist angle of $\theta \approx 0.18^\circ$ and a detector resolution in the original dataset of 1.36 nm/pixel (See Figure 5.3). The results are compared to the ab-initio theory in Figure 5.4. Although the experimental contrast is much lower, a remarkably good correspondence is achieved above 20 eV. This includes the contrast inversions, where domain boundaries and the AA site change from brighter than the Bernal (AB or BA) stacking (red) to darker (blue) and vice versa as a function of energy.

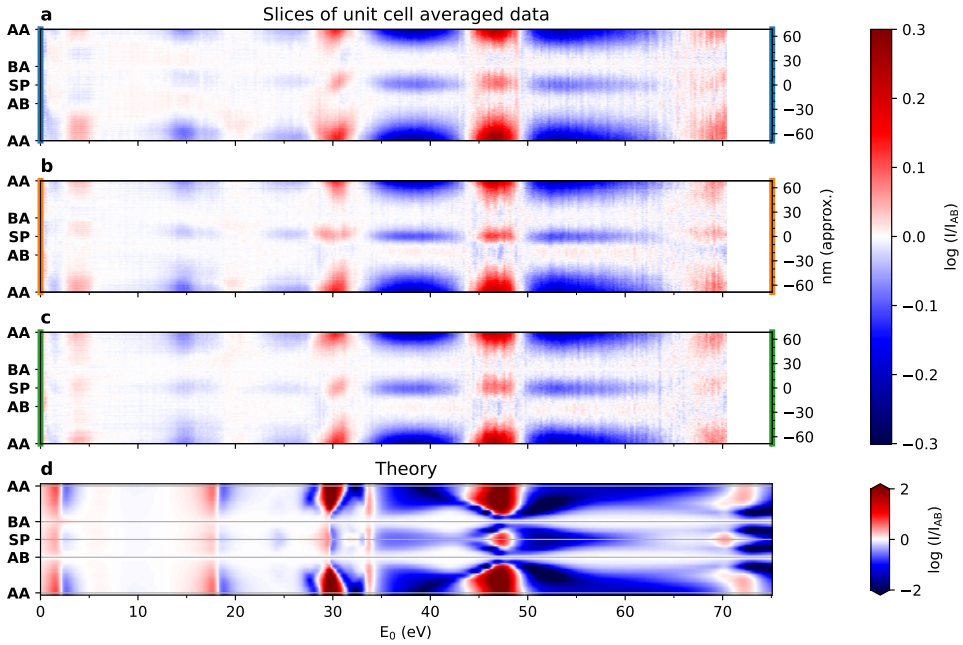

Figure 5.4: *Natural logarithm of the intensity of cuts through the averaged unit cells normalized with respect to the Bernal reflectivity in the three equivalent directions indicated with the same colors in Figure 5.3c (top three panels, corresponding to $\theta \approx 0.18^\circ$, detector resolution was 1.36 nm/pixel.) compared with (bottom panel) calculations of shifted equivalent stackings using the ab-initio theory, smoothed with a Gaussian with $\sigma = 0.2$ eV to account for experimental smoothing.*

Therefore, we conclude that at low twist angles, the moiré contrast is mainly caused by the different electron reflectivity of different local stackings and no significant phase contrast plays a role.

However, limitations of this approach in its current form are also immediately visible. Around contrast inversions, most prominently around 30 eV, it is clear from the asymmetric and different shapes in the three slices that the drift correction was not perfect, even relative to the large unit cell of this low twist angle. Note that the contrast inversions take place around the minima of the original spectra, where low intensity and energy spread of the electron source cause the most significant artefacts.

Notably, for lower energies, where ab-initio scattering mostly predicts a slight shift along E_0, experiment seems to indicate the inverse contrast, i.e. a shift in the opposite direction.

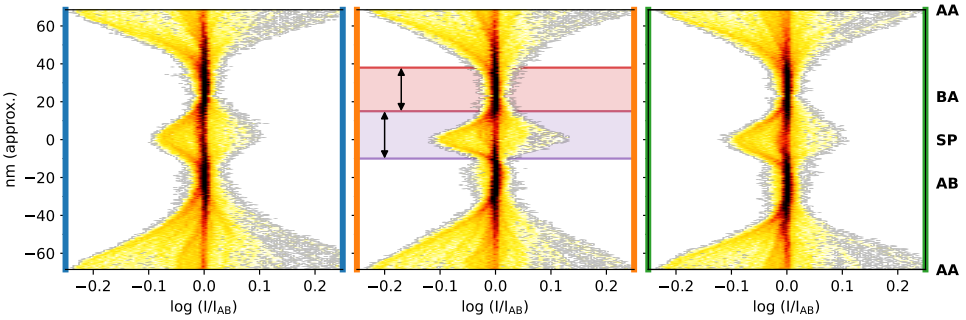

Figure 5.5: *2D-Histograms of the relative intensities (with respect to AB stacking) in Figure 5.4 for the different positions along the cuts, i.e. projected along E_0. Indicated in purple is the extracted domain boundary width, and in red the Bernal stacked area.*

Real space dimensions can also be extracted from these slices. The width around the indicated Bernal stacking in Figure 5.4 with approximately the same intensity is significantly larger than in the theoretical curves. This reaffirms that relaxation to Bernal stacking takes place, forming locally commensurate domains [120, 129] (which was also clear from the original data, such as in Figure 5.3**a,b**).

This broadening can be observed more clearly from the 2D-histogram of log-contrast values projected along E_0, as shown in Figure 5.5.

The width of the domain boundary is extracted from this, by measuring the length along the cut between AB and BA which has (significant) deviation from the Bernal stacking intensity for the full range of E_0, as indicated with the purple arrow in Figure 5.5. The observed width of about 25 nm is still much higher than the expected 7 nm, possibly by smearing during unit cell averaging, both intrinsic (thermal) broadening and electron optical broadening, and from imperfections of the extracted $\mathbf{u}(\mathbf{r})$.[6]

5.2.3 COMPARISON TO STRAIN DOMAIN BOUNDARIES IN GRAPHENE ON SIC

Next, we would like to compare the results on TBG from the previous section to the domain boundaries as observed in epitaxial graphene on silicon carbide. In the latter case, intrinsic stacking domains occur due to the lattice mismatch between the buffer layer and the graphene layers, as explored in Chapter 4 and 7. This means that in this system stacking contrast should occur due to tensile domain boundaries. This should hold both for hydrogen intercalated graphene on SiC, so-called quasi-freestanding bilayer graphene (QFBLG), and for epitaxial monolayer-on-buffer layer in the non-intercalated or de-intercalated material (EMLG). Indeed, domain boundaries in both systems cause contrast in BF-LEEM, as shown in Figure 5.6. Due to intrinsic disorder in this system

[6] Although the width along the slices in both other directions is larger, this is most probably due to the aforementioned remaining drift and therefore the minimum values can be assumed to be an upper bound.

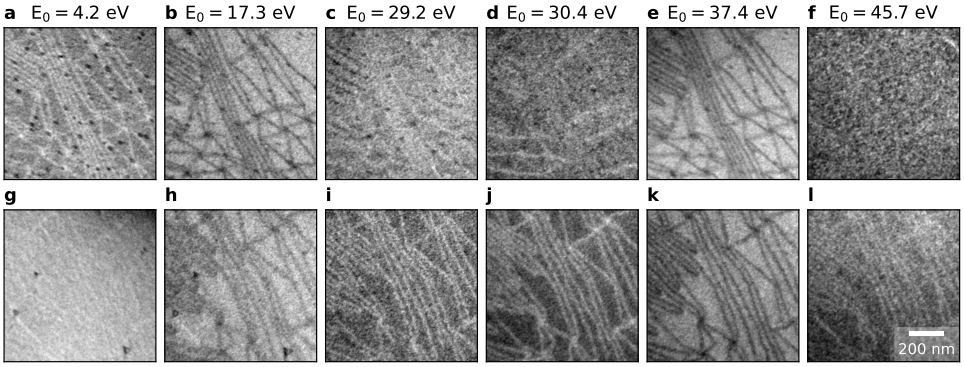

Figure 5.6: a-f, *Bright field stacking domain boundary contrast in quasi-freestanding bilayer graphene on SiC.* ***g-l,*** *The same for graphene on buffer layer on SiC (same area after hydrogen deintercalation). Both sets clearly show that depending on E_0, the domain boundaries can occur either bright or dark, although interestingly not at identical energies.*

however, no areas were imaged that are homogeneous enough to apply GPA to enable the same unit cell average analysis as applied in the previous section.

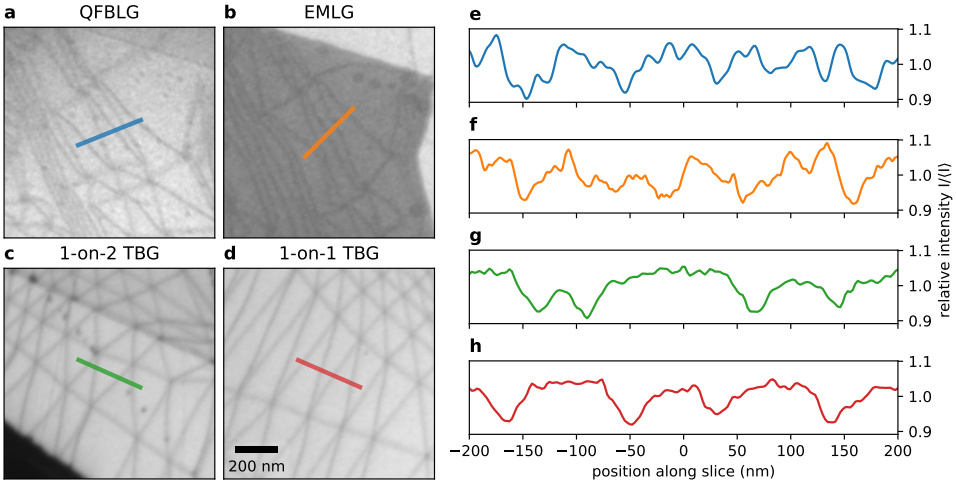

Figure 5.7: a-d, *Locations of the slices through stacking domain boundaries in several spectroscopic datasets. Scalebar applies to all panels and E_0 = 38 eV for all images and all images are individually optimized for contrast. The epitaxial graphene datasets have an original resolution of 2.2 nm/pixel, the TBG dataset a resolution of 3.7 nm/pixel.* ***e-h,*** *Normalized intensity along the slices indicated in respectively* ***a-d****.*

Nevertheless, we compare the contrast as a function of E_0 as observed in the epitaxial graphene samples to the twisted case by appropriate cross-sections through domain boundaries. The cross-sections, shown in Figure 5.7, were taken through multiple

domain boundaries, but without attempting to cross an AA site, as any remaining drift would invalidate such results.

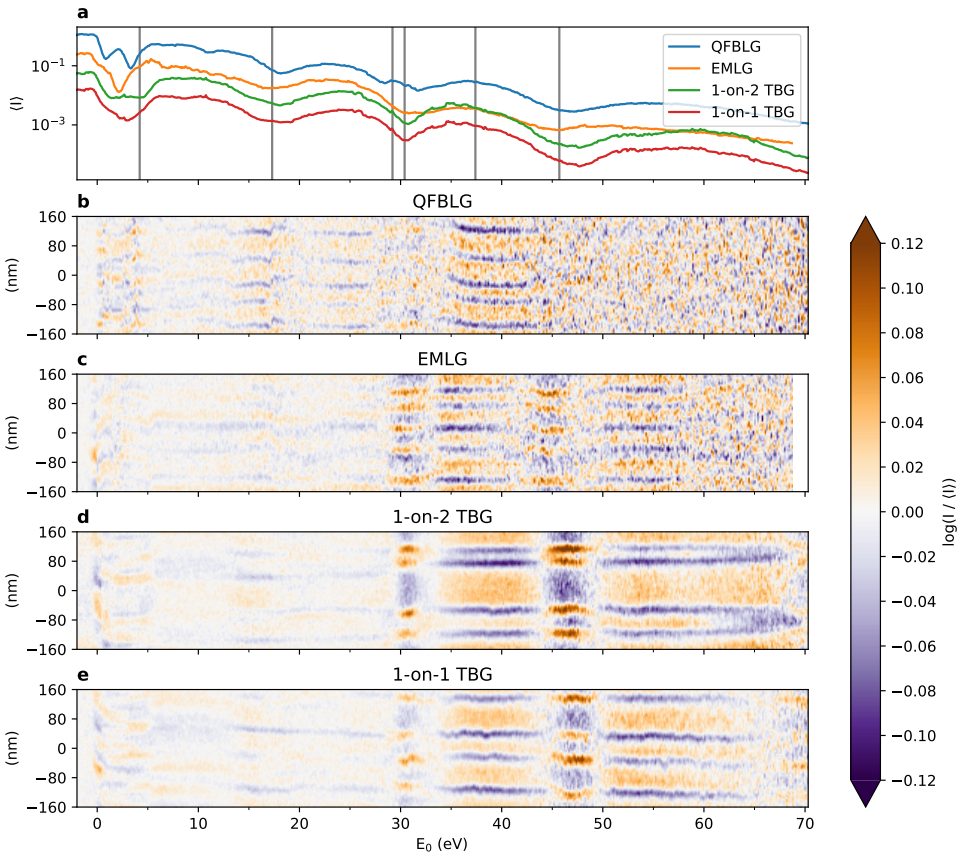

Figure 5.8: Comparison of domain boundaries with a single graphene top layer. ***a,*** *Average intensity along each slice* $\langle I \rangle$ *as a function of* E_0*, offset for clarity. Vertical lines indicate the images in Figure 5.6.* ***b-e,*** *Log-contrast, i.e. (natural) logarithm of the intensity relative to the slice average* $\langle I \rangle$ *as a function of* E_0*. The SiC slices (QFBLG and EMLG) are taken in the same area of Ref. [147], the TBG slices are taken from the data in Ref. [140]. Locations of the different slices are shown in Figure 5.7.*

The resulting energy-dependent average reflectivity $\langle I \rangle(E_0)$ along each slice is shown in Figure 5.8**a**, recovering the expected spectra for QFBLG, EMLG, bilayer graphene on hBN and trilayer graphene on hBN. The log-contrast $\log(I/\langle I \rangle)$ as a function E_0 along each slice is shown Figure 5.8**b-e**. Here, in addition to the regular flat field correction (as described in Chapter 3), a linear profile along the spatial direction is subtracted to compensate for remaining illumination inhomogeneity.

Contrast is remarkably similar for all systems shown, with dark (blue) domain boundaries for E_0 between 35 and 43 eV and contrast inversion above and below that, con-

sistent with the calculations, which show similar contrast inversions. For QFBLG and EMLG, the contrast washes out at higher E_0 (QFBLG above 45 eV, EMLG above 65 eV). However, this is an artefact most likely caused by insufficient integration time combined with incorrect focus tracking of the objective lens, causing the images to defocus at the high energies. Notably, the contrast below 30 eV is lower in EMLG than in the others, possibly due to the slightly different structure of the buffer layer compared to 'true' graphene layers in QFBLG and the TBG areas.

Some residual drift is present in the slices of each system, as the domain boundaries move collectively as a function of energy. Notably, some domain boundaries also move with respect to each other, e.g. the center two domain boundaries of 1-on-1 TBG around 39 eV. Such dynamics of the moiré pattern are in fact common and characterized more precisely in Chapter 6. By comparing the 1-on-1 TBG in Figure 5.8 to the unit cell averaged data in Figure 5.4, it becomes clear that the log-contrast for unit cell averaged data is about 1.5 times larger (0.2 peak-to-peak in Figure 5.8 versus 0.3 Bernal-to-peak in the unit cell averaged case).[7] Contrary to theory, all systems seem to consistently show at least some contrast for all energies lower than 30eV, although with varying strength and sign.

Domain boundaries in all four datasets are wider than the 6–11 nm predicted by simulations [19, 106], even when taking into account the non-perpendicular cuts. This suggests the data is again limited by electron optical reasons: either electron optical resolution of the measurements, or contribution of a phase component in addition to the pure amplitude component of the calculated stacking contrast to the image formation.

The 1-on-2 TBG data is remarkably similar to that of the other systems in this section, matching well to theory. The most evident difference in this system is the contrast between neighboring domains, which correspond to ABA and ABC stacking respectively, for example around 0, 10, 33 and 65 eV. This contrast between different Bernal and rhombohedral stackings will be explored in more detail in the next section.

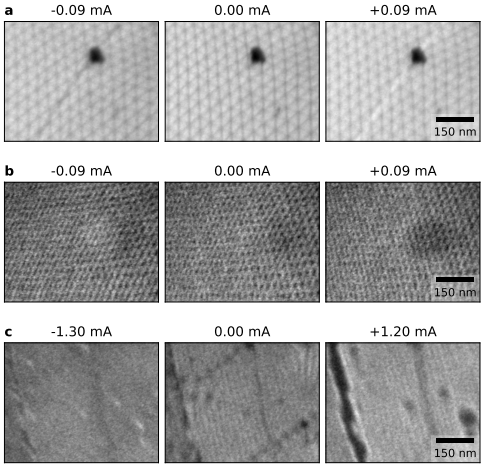

Figure 5.9: Defocus series. ***a,*** *Defocus series of TBG at $\theta \approx 0.18°$ at $E_0 = 36.5$ eV. The contrast of a diagonal line feature, presumably in the hBN substrate, inverts: from dark in underfocus to bright in overfocus.* ***b,*** *Defocus series of TBG at $\theta \approx 0.6°$ at $E_0 = 37.3$ eV. A round feature, presumably a bubble under the TBG, inverts contrast from bright in underfocus to dark in overfocus.* ***c,*** *Defocus series of graphene on SiC at $E_0 = 37.3$ eV. Several adsorbed carbohydrate residue particles change from bright in underfocus to dark in overfocus. Data taken on sample B as described in Chapter 7. Defocus is indicated above each panel in terms of objective lens excitation current relative to focus. Scalebars apply to all panels.*

[7] In terms of non-log contrast this corresponds to approximately a factor 1.2 peak-to-peak for the slices and 1.35 Bernal-to-peak for the unit cell averaged case.

Further evidence that the contrast in 1-on-1 TBG and graphene on SiC is pure amplitude contrast is given by the defocus series shown in Figure 5.9. If there would be a (strong) phase component to the contrast, this would invert as a function of defocus. Indeed, for all three defocus series, there are features present of which the contrast does invert as a function of defocus, but the domain boundaries do not show any signs of inverting contrast as a function of defocus in any of them. This confirms a pure amplitude contrast for domain boundaries both in TBG and in graphene on SiC.

5.3 BEYOND BILAYERS

While for bilayer graphene as explored in the previous sections, both possible Bernal stackings (AB / AC) are strictly equivalent as they are related by rotational symmetry (ignoring substrate effects), for trilayer and more layers, this equivalence is broken. In this section, the consequences of this for BF LEEM imaging of stacking domains multilayer (i.e. more than two layers) graphene are explored.

Bernal stacked trilayer graphene (ABA, occurring in natural graphite) has a distinct structure from rhombohedral graphene (ABC). The latter is hypothesized to possess interesting electronic properties, including flat bands [148–150] and a slightly different stacking energy [151, 152]. However, large areas of rhombohedral graphene turn out to be hard to create using standard stacking methods and even harder to stabilize, with samples typically showing a strong tendency to revert to Bernal stacking [120, 152].

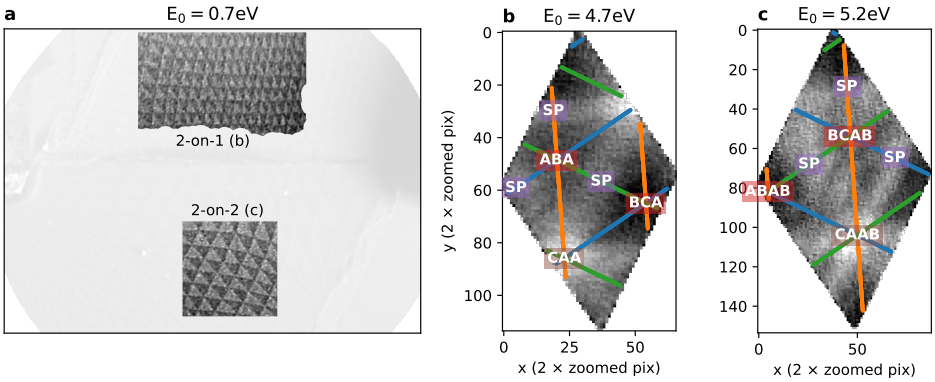

Figure 5.10: a, *BF LEEM image of an area of a TBG sample with both a 2-on-1 and a 2-on-2 area. The areas used for unit cell averaging are highlighted.* ***b,*** *Average unit cell for the 2-on-1 area at $E_0 = 4.7eV$ with the deduced stacking assignment indicated.* ***c,*** *Average unit cell for the 2-on-2 area at $E_0 = 5.2eV$ with the deduced stacking assignment indicated.*

Both minimally twisted multilayers and strained epitaxial graphene form a natural platform to study differences between different stackings, as areas of different stackings are inherently created in alternating patterns. Furthermore, they are topologically protected, since boundary nodes, which are as such sometimes referred to as 'twistons' in the twisted case, can only disappear by moving all the way to the edge of the sample. This behavior corresponds to full untwisting of the sample over relatively large length scales

for twisted samples. For the strainons in the strained epitaxial samples, the same holds, as the conservation is enforced by the binding to the substrate step edges and defects.

Aside from DF-LEEM, as described in Chapter 4 and used there to distinguish the different possible stackings in trilayer graphene on SiC, we will here explore the BF-LEEM characteristics of both domains and domain boundaries of different trilayer and quadlayer stackings.

As visible in Figure 5.8 (in the previous section), for 1-on-2, the domain boundaries yield very similar contrast to 1-on-1. This is expected, as the 'substrate' (an extra layer of graphene on hBN versus hBN in this case) has much less influence on the observed LEEM spectra than the top layers. However, some contrast between ABA and ABC stacking does appear when comparing to the bilayers, confirming the broken rotational symmetry.

Wildly different is the bright field contrast for samples where the twisted top layer consists of bilayer graphene, i.e. 2-on-1 and 2-on-2 TBG, as shown for $E_0 = 0.7$ eV in Figure 5.10**a**. Here, it is already clear that Bernal versus rhombohedral stacking dominates the contrast near mirror mode, visible as dark and bright triangles. These triangles are used to compute $\mathbf{u}(\mathbf{r})$ for unit cell averaging.

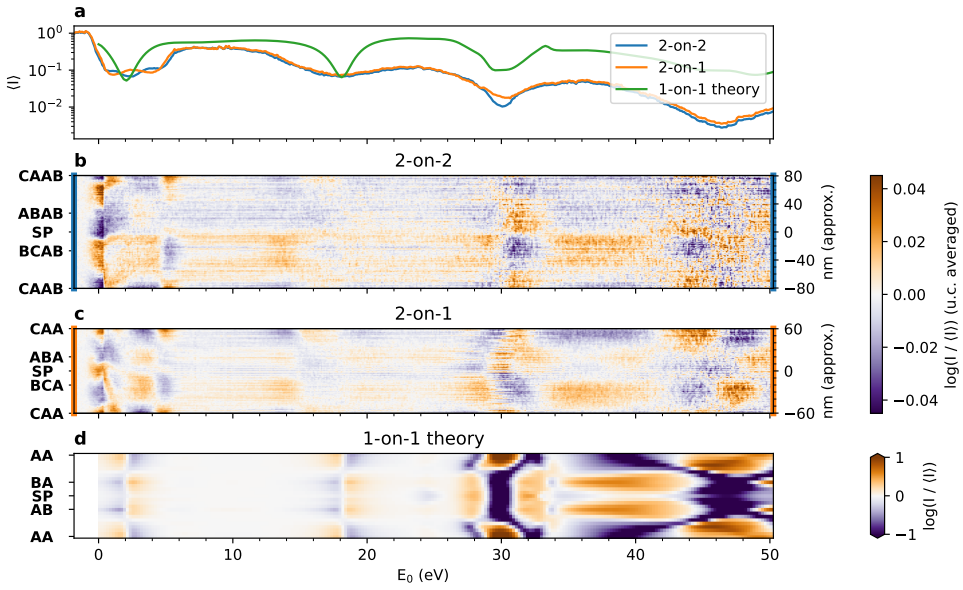

Figure 5.11: ***a,*** *Average intensity* $\langle I \rangle$ *as a function of* E_0 *for the areas indicated in Figure 5.10* ***a*** *and the average intensity for the computed theoretical reflectivities.* ***b,c,*** *Relative intensity of cuts through the averaged unit cells in the three directions indicated in Figure 5.10* ***b,c*** *for twisted bilayer-on-bilayer graphene. Data was taken at a magnification of 3.7 nm/pixel.* ***d,*** *Calculated relative intensity scaled by the average intensity for 1-on-1 bilayer.*

When looking at the resulting energy-dependent, unit cell averaged 2-on-1 and 2-on-2 data shown in Figure 5.11, the difference in contrast compared to the 1-on-X data in the previous section is clear. The overall contrast is much lower and the contrast between

ABA and ABC stacking dominates, although some (C)AA(B) and SP contrast is visible, for example around 5 eV.

5.3.1 2-ON-2 GRAPHENE LAYERS: PHASE CONTRAST

The results shown in the previous sections are fairly consistent with the calculations and therefore with pure amplitude contrast. However, something unexpected happens for 2-on-2 TBG data of a higher twist-angle, smaller unit cell area, such as in Figure 5.12.

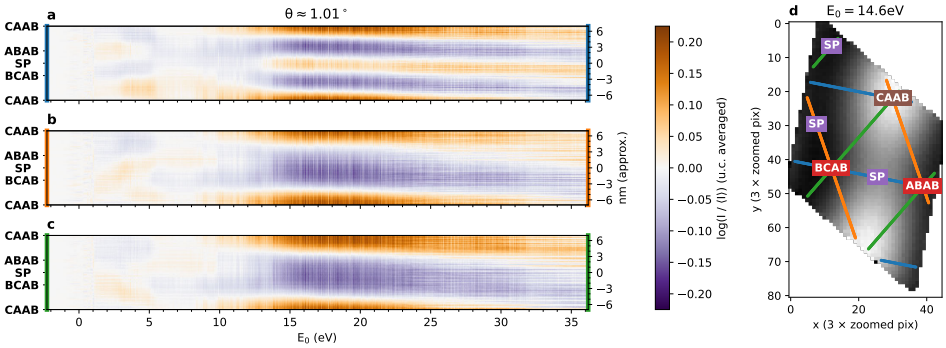

Figure 5.12: a-c, *Relative intensity of cuts through the averaged unit cells for twisted bilayer-on-bilayer graphene near the magic angle. Data was taken at a magnification of 0.9 nm/pixel. Note the difference in colorscale compared to Figures 5.11 and 5.13.* ***d,*** *Averaged unit cell with the cuts taken in* ***a-c*** *indicated.*

Although the size of this moiré is close to the resolution limit of the instrument, the contrast is very high and shows no inversions between ~ 10 eV and 36 eV. The observed contrast is the highest of all measurements presented in this work, peaking at $\frac{I_{\max}}{I_{\min}}\Big|_{E_0} \approx 1.5$ for a relatively wide region around $E_0 = 20$ eV.[8]

The stacking assignment as indicated in Figure 5.12**d** is speculative: it could as well be mainly caused by BCAB/ABAB contrast instead of the CAAB nodes yielding the main contribution to the contrast as was assumed there. The precise distinction seems impossible to make from this data due to the resolution limits of LEEM and the remaining astigmatism.

Nevertheless, the much higher contrast and lack of contrast inversion at this higher twist angle compared to the $\theta = 0.08$ data (shown for comparison for all three equivalent cuts in Figure 5.13), indicates phase contrast (where electrons reflecting off different parts of the unit cell interfere with each other) dominates for these higher twist angles in 2-on-2 TBG.

The proof of the pudding that the observed contrast for high twist angle 2-on-2 TBG is due to phase contrast would be a contrast inversion of the moiré pattern as a function of defocus. A defocus series is shown in Figure 5.14, but unfortunately the same small size of the moiré pattern that would enable phase contrast puts it right on the edge of

[8] $1.5 \approx \exp(0.42)$, i.e. the contrast of 1.5 corresponds to difference of 0.42 on the purple–orange color scales in the figures.

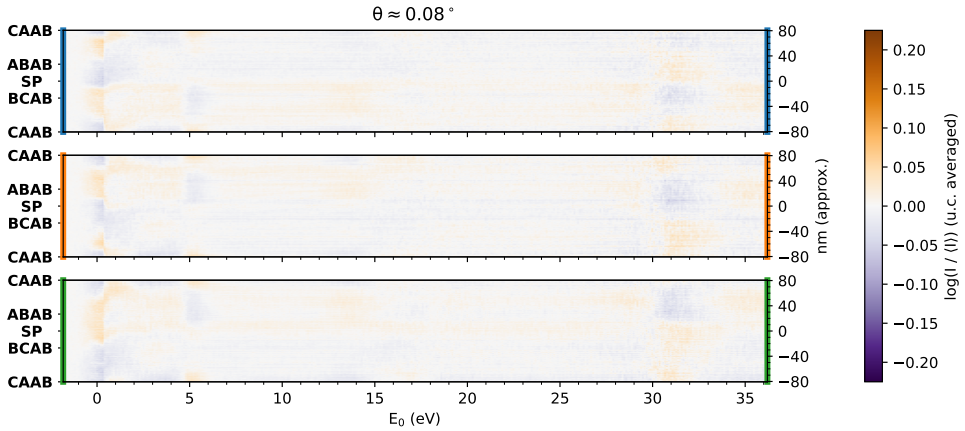

Figure 5.13: *Relative intensity of cuts through the averaged unit cells in the three directions indicated in Figure 5.10* ***c*** *for 2-on-2 TBG, with the colorscale matched to Figure 5.12 for comparison. Data was taken at a magnification of 3.7 nm/pixel.*

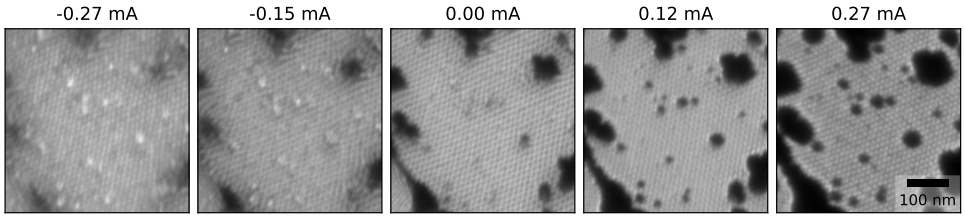

Figure 5.14: Defocus series of $\theta = 1.01°$ ***2-on-2 TBG.*** *Data taken at* $E_0 = 5.3$ *eV. Defocus relative to the center panel is expressed in mA excitation of the objective lens.*

the achievable resolution in the LEEM. Combined with the lack of clear reference points and some astigmatism makes it impossible to say for sure from this data if the contrast inverts or shifts or is completely stable. Although easily confused with remaining sample drift, it does however seem as if the contrast shifts around.

5.4 MOIRÉ METROLOGY

Beyond measuring the contrast of reflected low energy electrons of moiré patterns and determining the local twist angle, there is more that we can learn from imaging moiré patterns in such samples.

As described by Halbertal et al. for the case of 2-on-2 layer twisted graphene [151, 153], the shape of the domain boundaries can be directly related to any energy differences between different stackings and therefore can be used to *measure* (hence moiré *metrology*) these stacking energy differences.

In general, in a system with states of different energy that is in thermal equilibrium, the state with the lower energy will occur more often. The ratio between occupancy of the states is directly related to the energy difference by the Boltzmann factor. Although

the number of twistons in a twisted system, and therefore the number of alternating domains is conserved (ignoring edge cases), the size of the domains can change by movement of the domain boundaries.

However, the relative size of different stacking domains does not map directly to such a Boltzmann factor, as the energy cost per unit length of domain boundary has to be taken into account. What is more, this energy cost is dependent on the local angle between the domain boundary and the atomic lattice. Nevertheless, Halbertal et al. show that the generalized stacking fault energy (GSFE), the stacking energy as a function of relative displacement of lattices, can be directly related to the curvature κ of domain boundaries of the triangular domains, which they image using scanning near-field optical microscopy (SNOM). This methodology works for 2-on-2 TBG, but also for other materials.

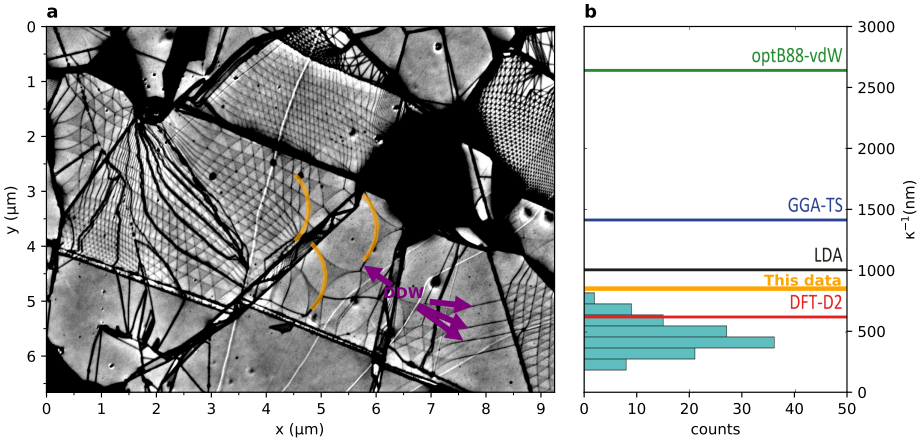

Figure 5.15: Moiré metrology. ***a,*** *BF-LEEM image of a 2-on-2 TBG area with very low twist angle (same device as ref. [135]). Domain boundaries in the 2-on-2 TBG areas are clearly visible, as is a slight contrast between ABAB and BCAB domains. In the very low twist angle areas, the curvature of the domain bounderies is very apparent. For three of them a matching orange arc with a curvature of* $\kappa^{-1} = 850$ *nm, is overlayed. Some double domain walls (DDW) are indicated with purple arrows.* ***b,*** *Measured curvatures using SNOM as a histogram with the predictions from different ab-initio calculation schemes indicated as lines, adapted from [151]. The curvature drawn in* ***a*** *is also indicated with an orange line.*

As shown in the preceding sections, LEEM can similarly image domains in diverse systems of heterostacks, providing another way to measure the shapes of these domain boundaries and therefore calibrate theoretical calculations of such stacking differences.

As calculations seem to suggest that both magnitude and direction of heterostrain influence the energy differences between different stackings, measuring larger areas of twisted heterostructures seems very worthwhile [152]. In such samples, varying strain can be characterized locally using GPA (as described in Ref. [21, 135, 151, 154]) and in conjunction the energy difference between the stackings can be determined by domain boundary curvature. This way, varying strain and energy difference can be connected

experimentally.

In Figure 5.15 a proof-of-concept of using LEEM to do such measurements is shown. Although the sample used only showed some areas of low enough twist angle to measure κ, it is already clear that we measure a value outside of the range of values that Halbertal et al. obtained as indicated by the histogram in Figure 5.15**b** and, interestingly, closer to theoretically predicted values using LDA, GGA-TS and optB88-vdW, but farther away from the one from DFT-D2 (for more details on the differences between these calculations, see the Methods section of Ref. [151]). Furthermore we observe double domain walls in the 2-on-2 TBG (for example the ones indicated with purple arrows in Figure 5.15), similar to observations by Halbertal et al., although we note that these did not occur in the 1-on-1 and 2-on-1 areas of the sample.

The possibilities for such measurements in a LEEM opens up a further research avenue: to explore the *dynamics* of the domain wall positions in such minimally twisted samples, similar to the work on higher twist angle data in Ref. [135]. By mapping the domain wall mobility as well as equilibrium curvatures as a function of temperature, it would be possible to not only explore the energy differences between the stackings, but also further characterize the stacking energy landscape.

5.5 CONCLUSION

In conclusion, we have shown that for large stacking domains in bilayer graphene, the local stacking in the domain walls and nodes is the primary BF-LEEM amplitude contrast mechanism for $E_0 \gtrsim 30$ eV. The contrasts observed in this energy range correspond very well to theoretical calculations, both for (low angle) 1-on-1 and 1-on-2 twisted bilayer graphene as well as for QFBLG and EMLG on silicon carbide, although the observed contrast is much lower due to the spatial resolution limitations of the experiment and thermal broadening.

Furthermore, we have applied similar methods to map the stacking contrast for 2-on-2 and 2-on-1 TBG. Here, for low angle data, the contrast is much lower, and mostly caused by contrast between the (meta-)stable Bernal and rhombohedral stackings, with domain boundaries only exhibiting minor contrast at some landing energies. Curiously, for $\theta \approx 1^\circ$, 2-on-2 TBG exhibits a much stronger contrast, stronger even than 1-on-1 TBG, suggesting that a phase contrast mechanism distinct from the local stacking contrast starts to become dominant.

The optimal landing energy range to image domain boundaries in a bilayer of graphene seems to be 30– 50 eV, where a strong amplitude contrast occurs and the intensity is still relatively high. For domain boundaries between deeper lying layers, the amplitude contrast at high values of E_0 is much lower, and the optimal energy to image the domains themselves is at very lower energies, 0 – 10 eV, where there is plenty of intensity and the work function difference causes relatively strong contrast. An exception holds for larger twist angles / smaller domains, where phase contrast is the dominant contrast mechanism causing strong contrast between 10 and 20 eV. We speculate that these trends are more generally applicable to stacking boundaries in Van der Waals heterostacks, beyond the graphene-graphene system alone: significant amplitude stacking contrast only for E_0 larger than the energy at which the first order diffraction spots appear, large deeper

lying domains most clearly imagable by slight work function differences and small domains dominated by phase contrast, especially for deeper lying stacking differences.

The contrast mechanisms as explored here are exploited to measure local strain and twist angle in TBG in Chapter 6 (Ref. [135]) and to explore relative strain and disorder in epitaxial graphene on SiC in Chapter 7.

Finally, we have shown the potential of using such contrast in twisted heterostacks to closely study the energy differences between different possible stackings.

5.6 OUTLOOK: POSSIBLE COMPUTATIONAL IMPROVEMENTS

Although several conclusions could be drawn from the unit cell averaged data in this chapter, it is also clear that there are still algorithmic limitations of the current implementation of the unit cell averaging, both in the unit cell averaging itself and in the adaptive Geometric Phase Analysis (GPA) used to obtain the displacement field $\mathbf{u}(\mathbf{r})$. As an outlook, I will here list several algorithmic improvements that could still be made to improve the data quality.

- Some residual drift plagues the unit cell cuts. Some of this is unavoidable in the current method, as due to different contrast mechanisms and height differences, the moiré pattern tends to move slightly different compared to larger features such as folds and adsorbates. It should however be possible to derive a final correction of the drift by minimizing asymmetry of the resulting cuts through the unit cell.

- Non-isotropic unit vectors for GPA can be used instead of the forced isotropic ones used now. This way, they would correspond to the average local deformation and limit distortion. Additionally, influences of the strain could be studied by comparing different direction cuts through the unit cell.

- GPA intrinsically introduces a convolution with a broadening kernel (in this work always Gaussian). In principle, this convolution can be deconvolved from the GPA result if the signal to noise ratio in the result is low enough. This increases the accuracy of the recovered $\mathbf{u}(\mathbf{r})$, especially in areas with gradients. However, due to SNR requirements and inherent inaccuracy of the unit cell averaging introduced by strongly changing unit cell sizes the improvement obtained using deconvolution might be limited.

- Deformation changes: We have seen the moiré lattice fluctuates. Therefore, instead of using a fixed $\mathbf{u}(\mathbf{r})$, compute $\mathbf{u}(\mathbf{r})$ for multiple different energies with high contrast and interpolate between those.

- Pixels on an edge of the unit cell are not treated perfectly, yielding severe edge effects. Therefore an overlap should be used to created a drizzled average slightly larger than the unit cell. To achieve the smallest such overlap, one should add pixels falling on the edge (i.e. for which the drop falls on at least one pixel with a coordinate outside the unit cell) to both sides of the unit cell to ensure coverage of these drizzle drops on both sides. An alternative would be to drizzle in fractional lattice vector coordinates instead of Cartesian coordinates, but this would yield more complicated computations and non-trivial drizzle drop shapes.

- The size and potentially also the shape of the drizzle drops can be optimized. The current choice for a 1-by-1 pixel square in the resulting averaged unit cell was easiest to implement, but probably not optimal.

REFERENCES

10. D. Momeni Pakdehi, J. Aprojanz, A. Sinterhauf, et al. Minimum Resistance Anisotropy of Epitaxial Graphene on SiC. *ACS Applied Materials & Interfaces* **10,** 6039–6045. doi:10.1021/acsami.7b18641 (2018).

11. A. M. Popov, I. V. Lebedeva, A. A. Knizhnik, Y. E. Lozovik & B. V. Potapkin. Commensurate–incommensurate phase transition in bilayer graphene. *Physical Review B* **84,** 045404. doi:10.1103/PhysRevB.84.045404 (2011).

12. C. Riedl, U. Starke, J. Bernhardt, M. Franke & K. Heinz. Structural properties of the graphene-SiC(0001) interface as a key for the preparation of homogeneous large-terrace graphene surfaces. *Physical Review B* **76,** 245406. doi:10.1103/PhysRevB.76.245406 (2007).

13. S. Kim, J. Ihm, H. J. Choi & Y.-W. Son. Origin of Anomalous Electronic Structures of Epitaxial Graphene on Silicon Carbide. *Physical Review Letters* **100,** 176802. doi:10.1103/PhysRevLett.100.176802 (2008).

17. J. Ravnik, I. Vaskivskyi, Y. Gerasimenko, et al. Strain-Induced Metastable Topological Networks in Laser-Fabricated TaS_2 Polytype Heterostructures for Nanoscale Devices. *ACS Applied Nano Materials* **2,** 3743–3751. doi:10.1021/acsanm.9b00644 (2019).

19. I. V. Lebedeva & A. M. Popov. Two Phases with Different Domain Wall Networks and a Reentrant Phase Transition in Bilayer Graphene under Strain. *Physical Review Letters* **124,** 116101. doi:10.1103/PhysRevLett.124.116101 (2020).

21. F. Mesple, A. Missaoui, T. Cea, et al. Heterostrain Determines Flat Bands in Magic-Angle Twisted Graphene Layers. *Physical Review Letters* **127,** 126405. doi:10.1103/PhysRevLett.127.126405 (2021).

25. R. Tromp, J. Hannon, A. Ellis, et al. A new aberration-corrected, energy-filtered LEEM/PEEM instrument. I. Principles and design. *Ultramicroscopy* **110,** 852–861. doi:10.1016/j.ultramic.2010.03.005 (2010).

27. R. M. Tromp, J. B. Hannon, W. Wan, A. Berghaus & O. Schaff. A new aberration-corrected, energy-filtered LEEM/PEEM instrument II. Operation and results. *Ultramicroscopy* **127,** 25–39. doi:10.1016/j.ultramic.2012.07.016 (2013).

37. T. A. de Jong, E. E. Krasovskii, C. Ott, et al. Intrinsic stacking domains in graphene on silicon carbide: A pathway for intercalation. *Physical Review Materials* **2,** 104005. doi:10.1103/PhysRevMaterials.2.104005 (2018).

88. T. A. de Jong. *pyGPA* 2021. doi:10.5281/zenodo.5589555.

95. K. V. Emtsev, A. Bostwick, K. Horn, et al. Towards wafer-size graphene layers by atmospheric pressure graphitization of silicon carbide. *Nature Materials* **8,** 203–207. doi:10.1038/nmat2382 (2009).

106. J. S. Alden, A. W. Tsen, P. Y. Huang, et al. Strain solitons and topological defects in bilayer graphene. *Proceedings of the National Academy of Sciences* **110,** 11256–11260. doi:10.1073/pnas.1309394110 (2013).

108. I. Martin, Y. M. Blanter & A. F. Morpurgo. Topological Confinement in Bilayer Graphene. *Physical Review Letters* **100,** 036804. doi:10.1103/PhysRevLett.100.036804 (2008).

114. R. M. Tromp & J. B. Hannon. Thermodynamics and Kinetics of Graphene Growth on SiC(0001). *Physical Review Letters* **102,** 106104. doi:10.1103/PhysRevLett.102.106104 (2009).

120. H. Yoo, R. Engelke, S. Carr, et al. Atomic and electronic reconstruction at the van der Waals interface in twisted bilayer graphene. *Nature Materials* **18,** 448–453. doi:10.1038/s41563-019-0346-z (2019).

122. L.-J. Yin, H. Jiang, J.-B. Qiao & L. He. Direct imaging of topological edge states at a bilayer graphene domain wall. *Nature Communications* **7,** 11760. doi:10.1038/ncomms11760 (2016).

124. T. A. de Jong, X. Chen, E. E. Krasovskii, et al. Low-Energy Electron Microscopy contrast of stacking boundaries: comparing twisted few-layer graphene and strained epitaxial graphene on silicon carbide. *under review.* https://arxiv.org/abs/2207.14616 (2022).

125. A. J. Van Bommel, J. E. Crombeen & A. Van Tooren. LEED and Auger electron observations of the SiC(0001) surface. *Surface Science* **48,** 463–472. doi:10.1016/0039-6028(75)90419-7 (1975).

126. J. B. Hannon, M. Copel & R. M. Tromp. Direct Measurement of the Growth Mode of Graphene on SiC(0001) and SiC (000 1 ¯). *Physical Review Letters* **107,** 166101. doi:10.1103/PhysRevLett.107.166101 (2011).

127. S. Tanaka, K. Morita & H. Hibino. Anisotropic layer-by-layer growth of graphene on vicinal SiC(0001) surfaces. *Physical Review B* **81,** 041406. doi:10.1103/PhysRevB.81.041406 (2010).

128. M. Kruskopf, D. M. Pakdehi, K. Pierz, et al. Comeback of epitaxial graphene for electronics: large-area growth of bilayer-free graphene on SiC. *2D Materials* **3,** 041002. doi:10.1088/2053-1583/3/4/041002 (2016).

129. S. Carr, D. Massatt, S. B. Torrisi, et al. Relaxation and domain formation in incommensurate two-dimensional heterostructures. *Physical Review B* **98,** 224102. doi:10.1103/PhysRevB.98.224102 (2018).

130. E. Annevelink, H. T. Johnson & E. Ertekin. Topologically derived dislocation theory for twist and stretch moiré superlattices in bilayer graphene. *Physical Review B* **102,** 184107. doi:10.1103/PhysRevB.102.184107 (2020).

131. J. Lin, W. Fang, W. Zhou, et al. AC/AB Stacking Boundaries in Bilayer Graphene. *Nano Letters* **13,** 3262–3268. doi:10.1021/nl4013979 (2013).

132. S. Turkel, J. Swann, Z. Zhu, et al. Twistons in a Sea of Magic. *arXiv:2109.12631 [cond-mat].* http://arxiv.org/abs/2109.12631 (2022) (2021).

133. S. Huang, K. Kim, D. K. Efimkin, et al. Topologically Protected Helical States in Minimally Twisted Bilayer Graphene. *Physical Review Letters* **121,** 037702. doi:10.1103/PhysRevLett.121.037702 (2018).

134. J. D. Verbakel, Q. Yao, K. Sotthewes & H. J. W. Zandvliet. Valley-protected one-dimensional states in small-angle twisted bilayer graphene. *Physical Review B* **103,** 165134. doi:10.1103/PhysRevB.103.165134 (2021).

135. T. A. de Jong, T. Benschop, X. Chen, et al. Imaging moiré deformation and dynamics in twisted bilayer graphene. *Nature Communications* **13,** 70. doi:10.1038/s41467-021-27646-1 (2022).

136. E. Krasovskii. Ab Initio Theory of Photoemission from Graphene. *Nanomaterials* **11,** 1212. doi:10.3390/nano11051212 (2021).

137. H. Hibino, S. Mizuno, H. Kageshima, M. Nagase & H. Yamaguchi. Stacking domains of epitaxial few-layer graphene on SiC(0001). *Physical Review B* **80,** 085406. doi:10.1103/PhysRevB.80.085406 (2009).

138. P. Schädlich, F. Speck, C. Bouhafs, et al. Stacking Relations and Substrate Interaction of Graphene on Copper Foil. *Advanced Materials Interfaces* **8,** 2002025. doi:10.1002/admi.202002025 (2021).

139. S. M. Schramm, A. B. Pang, M. S. Altman & R. M. Tromp. A Contrast Transfer Function approach for image calculations in standard and aberration-corrected LEEM and PEEM. *Ultramicroscopy* **115,** 88–108. doi:10.1016/j.ultramic.2011.11.005 (2012).

140. T. de Jong, T. Benschop, X. Chen, et al. *Data underlying the paper: Imaging moiré deformation and dynamics in twisted bilayer graphene.* (4TU.ResearchData, 2021). doi:10.4121/16843510.

141. T. Benschop*, T. A. de Jong*, P. Stepanov*, et al. Measuring local moiré lattice heterogeneity of twisted bilayer graphene. *Physical Review Research* **3,** 013153. doi:10.1103/PhysRevResearch.3.013153 (2021).

142. J. A. Slezak, J. Lee, M. Wang, et al. Imaging the impact on cuprate superconductivity of varying the interatomic distances within individual crystal unit cells. *Proceedings of the National Academy of Sciences* **105,** 3203–3208. doi:10.1073/pnas.0706795105 (2008).

143. M. J. Lawler, K. Fujita, J. Lee, et al. Intra-unit-cell electronic nematicity of the high-Tc copper-oxide pseudogap states. *Nature* **466,** 347–351. doi:10.1038/nature09169 (2010).

144. A. S. Fruchter & R. N. Hook. Drizzle: A Method for the Linear Reconstruction of Undersampled Images. *Publications of the Astronomical Society of the Pacific* **114,** 144–152. doi:10.1086/338393 (2002).

145. A.-J. Quist. *Superresolution in Low Energy Electron Microscopy using drizzle* BSc thesis (Leiden University, 2020). https://hdl.handle.net/1887/133077.

146. T. A. de Jong. *Graphene stacking domains code* 2022. https://github.com/TAdeJong/graphene-stacking-domains-code.

147. T. A. de Jong, J. Jobst & E. E. Krasovskii. *Data underlying the paper: Intrinsic stacking domains in graphene on silicon carbide: a pathway for intercalation* (4TU.ResearchData, 2018). doi:10.4121/uuid:a7ff07f4-0ac8-4778-bec9-636532cfcfc1.

148. D. Pierucci, T. Brumme, J.-C. Girard, et al. Atomic and electronic structure of trilayer graphene/SiC(0001): Evidence of Strong Dependence on Stacking Sequence and charge transfer. *Scientific Reports* **6,** 33487. doi:10.1038/srep33487 (2016).

149. H. Henck, J. Avila, Z. Ben Aziza, et al. Flat electronic bands in long sequences of rhombohedral-stacked graphene. *Physical Review B* **97,** 245421. doi:10.1103/PhysRevB.97.245421 (2018).

150. D. Marchenko, D. V. Evtushinsky, E. Golias, et al. Extremely flat band in bilayer graphene. *Science Advances* **4,** eaau0059. doi:10.1126/sciadv.aau0059 (2018).

151. D. Halbertal, N. R. Finney, S. S. Sunku, et al. Moiré metrology of energy landscapes in van der Waals heterostructures. *Nature Communications* **12,** 242. doi:10.1038/s41467-020-20428-1 (2021).

152. R. Guerrero-Avilés, M. Pelc, F. Geisenhof, T. Weitz & A. Ayuela. Relative Stability of Bernal and Rhombohedral Stackings in Trilayer Graphene under Distortions. *arXiv:2110.06590 [cond-mat].* http://arxiv.org/abs/2110.06590 (2022) (2021).

153. V. V. Enaldiev, V. Zólyomi, C. Yelgel, S. J. Magorrian & V. I. Fal'ko. Stacking Domains and Dislocation Networks in Marginally Twisted Bilayers of Transition Metal Dichalcogenides. *Physical Review Letters* **124,** 206101. doi:10.1103/PhysRevLett.124.206101 (2020).

154. D. Halbertal, S. Shabani, A. N. Passupathy & D. N. Basov. Extracting the Strain Matrix and Twist Angle from the Moiré Superlattice in van der Waals Heterostructures. *ACS Nano* **16,** 1471–1476. doi:10.1021/acsnano.1c09789 (2022).